

Measurements and Modeling of Pore-Pressure Gradients in the Swash Zone Under Large-Scale Laboratory Bichromatic Waves

Kranenburg, J. W.M.; Pauli, T.; Jacobsen, N. G.; van der Werf, J. J.; Dionisio Antonio, S.; Campmans, G. H.P.; Reniers, A. J.H.M.; Hulscher, S. J.M.H.

DOI

[10.1029/2022JC019577](https://doi.org/10.1029/2022JC019577)

Publication date

2023

Document Version

Final published version

Published in

Journal of Geophysical Research: Oceans

Citation (APA)

Kranenburg, J. W. M., Pauli, T., Jacobsen, N. G., van der Werf, J. J., Dionisio Antonio, S., Campmans, G. H. P., Reniers, A. J. H. M., & Hulscher, S. J. M. H. (2023). Measurements and Modeling of Pore-Pressure Gradients in the Swash Zone Under Large-Scale Laboratory Bichromatic Waves. *Journal of Geophysical Research: Oceans*, 128(12), Article e2022JC019577. <https://doi.org/10.1029/2022JC019577>

Important note

To cite this publication, please use the final published version (if applicable).
Please check the document version above.





Copyright

Other than for strictly personal use, it is not permitted to download, forward or distribute the text or part of it, without the consent of the author(s) and/or copyright holder(s), unless the work is under an open content license such as Creative Commons.

Takedown policy

Please contact us and provide details if you believe this document breaches copyrights.
We will remove access to the work immediately and investigate your claim.

Measurements and Modeling of Pore-Pressure Gradients in the Swash Zone Under Large-Scale Laboratory Bichromatic Waves

J. W. M. Kranenburg^{1,2} , T. Pauli^{1,3}, N. G. Jacobsen⁴, J. J. van der Werf^{1,5}, S. Dionisio Antonio¹, G. H. P. Campmans¹ , A. J. H. M. Reniers⁶ , and S. J. M. H. Hulscher¹ 

¹University of Twente, NB Enschede, The Netherlands, ²Now at Deltares, Delft, The Netherlands, ³Now at Nebest BV, Amersfoort, The Netherlands, ⁴Vattenfall, København, Denmark, ⁵Deltares, Delft, The Netherlands, ⁶Delft University of Technology, Delft, The Netherlands

Key Points:

- New field-scale laboratory measurements of pore pressures in the swash zone in a fine sand bed have been conducted
- An analytical model based on Fourier decomposition models the pore pressures and gradients well
- The vertical pressure gradient can have an important impact on the Shields parameter, thereby influencing sediment transport

Correspondence to:

J. W. M. Kranenburg,
joost.kranenburg@deltares.nl

Citation:

Kranenburg, J. W. M., Pauli, T., Jacobsen, N. G., van der Werf, J. J., Dionisio Antonio, S., Campmans, G. H. P., et al. (2023). Measurements and modeling of pore-pressure gradients in the swash zone under large-scale laboratory bichromatic waves. *Journal of Geophysical Research: Oceans*, 128, e2022JC019577. <https://doi.org/10.1029/2022JC019577>

Received 1 FEB 2023

Accepted 6 AUG 2023

Author Contributions:

Conceptualization: J. W. M. Kranenburg, N. G. Jacobsen, J. J. van der Werf

Formal analysis: J. W. M. Kranenburg, T. Pauli, N. G. Jacobsen

Funding acquisition: J. J. van der Werf, A. J. H. M. Reniers, S. J. M. H. Hulscher

Investigation: J. W. M. Kranenburg, T. Pauli, N. G. Jacobsen, S. Dionisio Antonio

Methodology: J. W. M. Kranenburg, T. Pauli, N. G. Jacobsen, J. J. van der Werf

Project Administration: J. J. van der Werf, S. J. M. H. Hulscher

Software: J. W. M. Kranenburg, T. Pauli

Supervision: J. W. M. Kranenburg, N. G. Jacobsen, J. J. van der Werf, G. H. P. Campmans, A. J. H. M. Reniers, S. J. M. H. Hulscher

© 2023. The Authors.

This is an open access article under the terms of the [Creative Commons Attribution License](https://creativecommons.org/licenses/by/4.0/), which permits use, distribution and reproduction in any medium, provided the original work is properly cited.

Abstract The present work presents physical laboratory measurements of surface elevation and pore water pressures in a fine sand bed under bichromatic waves in a large-scale laboratory experiment. This was done at three cross-shore locations in the swash zone, with pressures being measured at different depths in the bed. The measurements show that the pore pressure signal decays and shifts with increased depth. These measurements are used to validate a practical model, based on the theory of Yamamoto et al. (1978, <https://doi.org/10.1017/S0022112078003006>) and Guest and Hay (2017, <https://doi.org/10.1002/2016JC012257>). The model corresponds well with the measurements ($nRMSE < 0.2$ and $R^2 > 0.95$ for most probes) and shows that a frequency-based model can reproduce the pressures in the bed, despite the bed being exposed during dry periods. Furthermore, the model provides the opportunity to calculate pressure gradients, both throughout the bed and at the bed surface. These modeled pressure gradients at the bed surface show that the vertical pressure gradient can have an important impact on the Shields parameter, thereby influencing sediment transport.

Plain Language Summary When waves run up and down the beach they can influence the pressure in the sand. In this work, we have measured pressures in the beach at different depths. A difference in pressure at different depths can lead to forces on the sand particles which make it easier or harder for the sand to move. The results show that at deep locations, the pressure varies slowly and a little later compared with pressures close to the beach surface. We also calculated the pressures with a model, which could predict the measured pressures very well. The model also shows that large differences in pressure exist at the bed surface.

1. Introduction

The swash zone is the region of the beach where waves run up and down the beach, connecting the submerged bed of the surf zone with the dry part of the beach. Here, the hydrodynamical forcing that drives sediment transport is not only controlled by what happens above the bed surface but, due to the porous nature of the sediment bed, is also influenced by interactions between the subsurface and surface flow (Masselink & Li, 2001). These interactions can manifest themselves as exchanges in mass and momentum through seepage (exfiltration and infiltration) and can ultimately influence the forcing on sediment grains, and thus affect sediment transport and morphodynamics (Baldock & Holmes, 1998; Butt et al., 2001; Horn, 2006).

For fine-grained beaches, the vertical ex-/infiltration velocities are small compared with the wave-related orbital velocities. Therefore, the effect on the overground flow is small compared with larger grains, as the small pores require larger pressure gradients to drive the flow due to the flow resistance (Masselink & Li, 2001). However, the small grains are more easily influenced by small changes in the near-bed hydrodynamics, such as for instance externally generated turbulence (Fredsoe et al., 2003). One important effect is that the seepage affects the shape of the boundary layer, which in turn influences the bed shear stress. This was studied experimentally by Conley and Inman (1994), who showed that infiltration leads to higher near-bed velocities and larger bed shear stresses (thinning of the wave boundary layer), while exfiltration had the opposite effect (thickening of the wave boundary layer). Later, Lohmann et al. (2006) investigated the role of turbulence in detail using Large Eddy Simulations. Along with similar implications for the bed shear stress as Conley and Inman (1994), they also showed that infiltration decreased turbulent flow fluctuations near the bed, whereas exfiltration increased these fluctuations. Another important effect is that local pressure gradients effects the immersed particle

Visualization: J. W. M. Kranenborg
Writing – original draft: J. W. M. Kranenborg
Writing – review & editing: J. W. M. Kranenborg, T. Pauli, N. G. Jacobsen, J. J. van der Werf, G. H. P. Campmans, A. J. H. M. Reniers, S. J. M. H. Hulscher

weight, leading to an apparent lower particle weight during exfiltration and a higher particle weight during infiltration (Baldock & Holmes, 1998; Francalanci et al., 2008). Butt et al. (2001) showed that grainsize plays an important role where, at smaller grainsizes, the effect of incorporating infiltration/exfiltration in their model was to enhance offshore transport and inhibit onshore transport. They suggest that at smaller grainsizes, the stabilizing/destabilizing effect, such as the modified effective weight, are dominant over boundary layer effects. In order to arrive at an improved understanding of these contributions to the net sediment transport in the swash zone, it is important to understand how incident waves influence the pressure and pressure gradient in the top layer of the soil.

Pressure gradients in the bed result from the finite wavelength of the water waves. Their behavior is influenced by the elasticity of the bed and the pore fluid (Biot, 1941; Yamamoto et al., 1978). This elasticity means that the pressure amplitude attenuates and the phasing shifts, strengthening with increased depth under the bed. Furthermore, at a given depth higher frequency components experience stronger attenuation and larger phase shifts than lower frequencies. This frequency-dependent attenuation and phase shifting ultimately results in gradients in the pressure field, where the strength of the attenuation and shifting is dependent on the physical properties of the bed, particularly the degree of saturation of the soil (Guest & Hay, 2017). The higher the degree of saturation, the lower the phase lag (Mory et al., 2007; Yamamoto et al., 1978). This degree of saturation in beaches depends on different factors, such as the depth below the surface and local wave and tide conditions. In the swash zone, air can enter the beach during the periods when the beach is dry. Furthermore, water that infiltrates the beach is not fully saturated and carries air bubbles with every infiltration event (Heiss et al., 2014), and also biological processes within the bed can produce gas and contribute to the air content (Horn, 2002). This means that the air content of the beach, and therefore the pressure behavior, can vary between different locations and seasons due to biological activity.

Previously, there have been measurement campaigns featuring a vertical array of pressure sensors to investigate pressure propagation in the surf and swash zones, both in the field and in laboratory environments. On natural beaches, pressure gradients have been observed in many such studies, associated with different sediment and wave characteristics (e.g., Turner and Nielsen (1997); Raubenheimer et al. (1998); Baldock et al. (2001); Mory et al. (2007); Pedrozo-Acuña et al. (2008); Guest and Hay (2017); Stark et al. (2022)). The measurements of Raubenheimer et al. (1998) did not show considerable phase shifting at a natural beach consisting of fine sand. However, the later studies by Pedrozo-Acuña et al. (2008) (gravel), Guest and Hay (2017), (mixed sand and gravel) and Stark et al. (2022) (medium to coarse sand) did find phase shifting in their results. Sumer et al. (2011, 2013) also measured the pressure gradients at multiple cross-shore locations for small-scale solitary and regular monochromatic waves, showing that the pressure gradients had a significant influence on the bed shear stress and sediment entrainment, also in the swash.

The recent recasting by Guest and Hay (2017) of the Yamamoto et al. (1978) model provides an elegant, one-parameter model to study the importance of phase shifting and attenuation. However, this model has not yet been used for studying pressures (and their gradients) in the swash-zone of sandy beaches. Furthermore, given the intermittent wetting and drying of the bed surface, it is unclear whether a model based on a superposition of components, each following the theory of Yamamoto et al. (1978) and Guest and Hay (2017), is valid in the swash zone at all, given that these models assume a continuously inundated and horizontal bed.

To investigate these issues, novel field-scale laboratory measurements of pore pressures at different depths were conducted, co-located with measurements of surface elevations and flow velocities. This was done for a sandy beach, similar to the Raubenheimer et al. (1998) but in a swash setting, and Sumer et al. (2011, 2013) but using larger, field-scale waves. Furthermore, since bed properties such as saturation can vary spatially, we conduct these measurements at three different cross-shore locations simultaneously. Additionally, we investigate the capability of the frequency-based analytical theory of Guest and Hay (2017) to model the pressure response at these locations, keeping in mind that the swash motion leaves the beach uncovered at times. The model can then be used to calculate pressure gradients in the top layer of the bed, which we use to investigate how vertical pressure gradients could influence the Shields number.

The paper first describes the experimental setup, analytical model and how these will be compared in Section 2. The results from the measurements, the model and its comparison are subsequently presented in Section 3. These results are then discussed in Section 4, after which we present the main conclusions in Section 5.

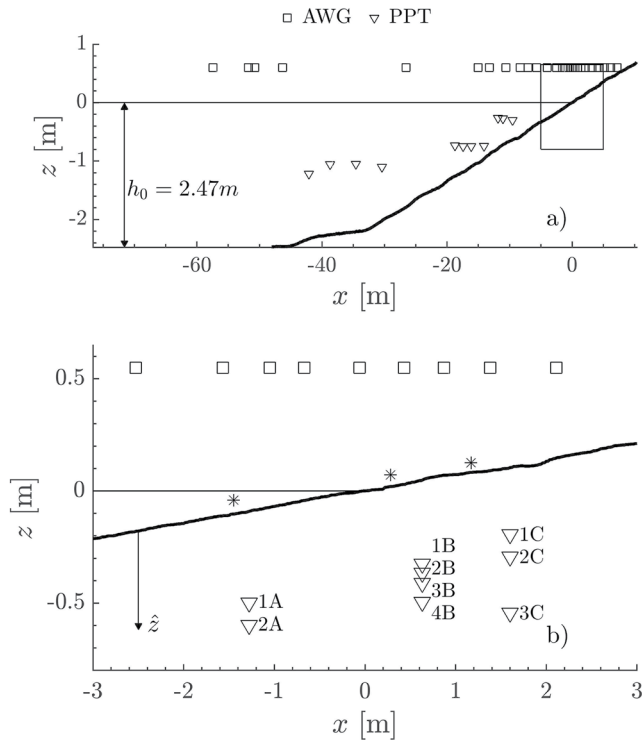


Figure 1. Overview of the initial bed level and instrument locations. Panel *a* shows the full flume and panel *b* shows a small section around the still water line. The squares, triangles and stars indicate the locations of wave gauges, pressure sensors and ADV's (velocity) respectively. The numbers show the indexing used to denote the different pressure sensors (see Table 1 for their locations). The pressure sensors in the water column in panel (a) were used for other experiments, not for measuring pore pressures.

2. Methodology

2.1. Experiment Setup

The experiments were conducted as part of the *Shaping The Beach* (Van der Werf et al., 2019) experimental campaign, at the large-scale CIEM facility of Universitat Politècnica de Catalunya in Barcelona. The flume is 100 m long, 3 m wide and 4.5 m deep and was filled with water with a depth $h_0 = 2.47$ m at the wave paddle. The depth-coordinate z is defined positively upward from the still water line. The cross-shore coordinate x is defined positively landward from the initial shoreline position. From the paddle end, the bottom of the flume is flat for 35.5 m, where the toe of the beach is located. From this point, the beach slopes upward with an initial slope of 1:15. The initial shoreline was situated at $x = 0$ m, roughly 77 m from the paddle (see Figure 1). The beach consisted of fine sand with $D_{10} = 0.15$ mm, $D_{50} = 0.25$ mm, and $D_{90} = 0.37$ mm, and a density of $\rho_s = 2,650$ kg/m³.

The experiment consisted of bichromatic waves with wave heights $H_1 = H_2 = 0.325$ m, group period $T_g = 21.37$ s and wave periods $T_1 = 2T_g/11$, $T_2 = 2T_g/13$. The target surface elevation signal η is thus

$$\eta = H_1 \cos(2\pi t/T_1) + H_2 \cos(2\pi t/T_2), \quad (1)$$

where t is time. This signal is designed such that the signal repeats every two wave groups with $T_r = 2T_g$. The resulting effective short-wave frequency is $T_s = 2T_g/12 = 3.56$ s, meaning there are six waves in every wave group.

For the experiment we define z as the global vertical coordinate. Additionally, for simplicity in the equations, we introduce \hat{z} to indicate the depth coordinate. With $z_b(x)$ being the location of the bed at the start of the measurements, we can thus link the coordinates with $\hat{z} = z_b - z$, such that $\hat{z} = 0$ m corresponds to the initial bed level.

2.1.1. Instrumentation

The setup of the instrumentation is shown in Figure 1. The experiment featured an array of Acoustic Wave Gauges (AWG) for measuring the water depth, Acoustic Doppler Velocimetry probes (ADV) for measuring velocities, Pore Pressure Transducers (PPT) of type STS ATM/N for measuring pressure, a profiler for measuring bed profiles before and after each run, and an array of other instruments not used in this study. The AWGs were installed in the swash zone at approximately 50 cm intervals. The measured surface elevations η are defined relative to the initial water level or, at initially dry locations, the dry bed profile as measured by the profiler (see Sanchez-Arcilla and Caceres (2018) for details on the profiler). We also define h as the total water depth. The ADVs were installed 3 cm above the local bed position at the beginning of the run. All instruments were synched through the CIEM equipment and were synched using a synchronisation pulse at the start of the run. The profiler was used to measure the bed profile after each 30-min wave session, and has a 1 cm vertical accuracy. Here it is important to consider that the profiler transect is in the middle of the flume, whereas the other probes were located closer to the flume wall. This means that there are discrepancies between the local bed levels at the probes and the measured profile.

Before the PPTs were buried, the opening of each probe was covered with a thin piece of cloth to keep sediment from entering the probe. Initially, four PPTs were buried at the three cross-shore locations, where they were attached to poles holding the probes in place. The burial depth of the probes was decided by estimating an expected profile evolution and burying them below this expected erosion level. The top three probes were spaced out by approximately 5 cm, and the lower probe was put deeper, as far as the equipment around the burial section would allow. Note that for all locations, the probes were buried at a depth where they were always covered with water to ensure continuous measurements. The precise depth of the buried sensors can be seen in Table 1.

Prior to the measurements used in this paper, 64 other 30-min runs with bichromatic and full wave spectra were conducted, compacting the sediment. The time in between trials was roughly 20 min, during which the flume

Table 1
Location and Depth of Pressure Sensors at the Start of the Measurements

| Sensor no. | Location A (surf) | | Location B (-) | | | | Location C (swash) | | |
|------------|-------------------|------|----------------|------|-------|------|--------------------|-----|------|
| | 1 | 2 | 1 | 2 | 3 | 4 | 1 | 2 | 3 |
| Depth (m) | 0.40 | 0.50 | 0.35 | 0.39 | 0.435 | 0.52 | 0.3 | 0.4 | 0.65 |

Note. Here the depth is denoted relative to the initial bed profile, in accordance with Figure 1.

could return to a calm state and the bed profile was measured. Just before the run analyzed in this paper, the top layer of the beach was manually reshaped to its initial profile. Unfortunately, due to one malfunctioning probe and two probes being exposed early in the experiments, the data from these probes is not used (these probes are not shown in Figure 1).

2.1.2. Data Treatment

An overview of the main data treatment steps is shown in Figure 2. The acoustic wave gauges displayed spurious oscillations with a frequency of approximately 10 Hz, which was removed using a low-pass filter with a cut-off frequency of $f = 8$ Hz, similar to Van der Zanden et al. (2019). The PPT sensors (measuring at 100 Hz) were first calibrated by filling the flume to two different water levels, measured at the paddle, ($h_{paddle} = 2.47$ m and $h_{paddle} = 2.665$ m) and measuring the hydrostatic water pressure under these stagnant conditions. For the rest of the study we are mainly interested in the pressure \tilde{p} in excess of the hydrostatic pressure potential. We define this pressure in the same way as Yeh and Mason (2014):

$$\tilde{p}(\hat{z}) = p(\hat{z}) - \rho_w g(\hat{z} - z_b), \quad (2)$$

where p is the total pressure.

Pressure gradients were estimated at the midpoint between two sensors by

$$\partial_z \tilde{p} = \frac{\tilde{p}_{deep} - \tilde{p}_{shallow}}{\hat{z}_{deep} - \hat{z}_{shallow}}. \quad (3)$$

Due to the different instruments placed in the flume, the cross-shore locations of the AWG and PPT probes are not identical. To minimize the effect this has on the results, the time delay between the PPT location and its AWG probe was estimated by measuring the time lag between neighboring AWG probes using cross-correlation, and interpolating this time lag to the PPT location.

The ADV probes measured the velocity at a frequency of 100 Hz. The raw signal was noisy, and the dry periods interrupted the otherwise continuous signal. Therefore, the raw signal was smoothed using a Gaussian smoothing operation with a window size of 10. Furthermore, the dry periods were identified and removed from the signal.

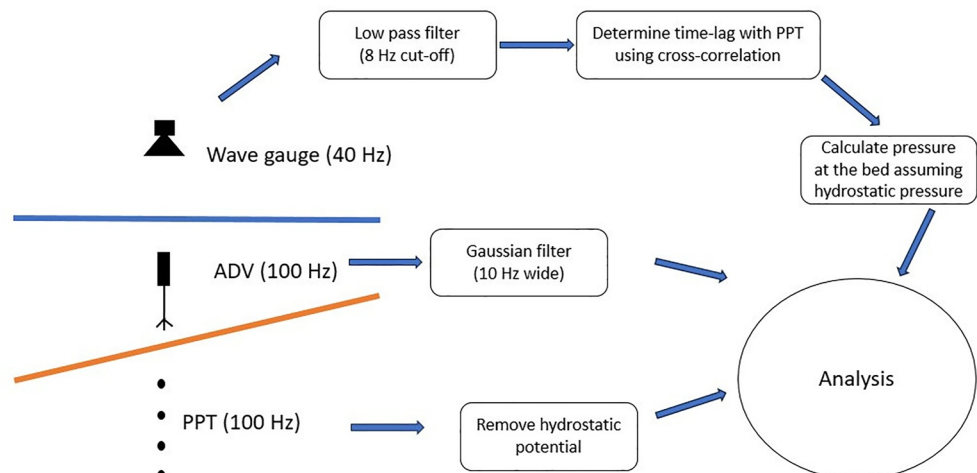


Figure 2. Schematic overview of the main data processing steps.

The transient build up of pressure due to the gradual increase of the groundwater setup in the beach means that the experiments initially are not in equilibrium. Therefore, all intraswash analyses and modeling is done on a subset of the data, ranging namely $t = 1,000\text{--}1,800$ s. This interval was determined after visual inspection of the pressure time series, and was chosen to exclude the initial transient increase of mean pressure. For this reason, any build-up effects on the measured pressure and pressure gradients should be negligible.

2.2. Analytical Model

The analytical model is based on the theory of Biot (1941), which assumes an isotropic soil-water mixture and Darcy-type porous flow. Importantly, the soil is not necessarily fully saturated, meaning that air bubbles can make the pore fluid compressible. Also the soil skeleton itself is assumed to behave as a linear elastic material. Following Biot (1941), multiple subsequent works have aimed to model stresses and pressures in the soil under waves (see Table 10.1 in Sumer and Fredsøe (2002)). Most notable are the theories by Yamamoto et al. (1978) and Hsu and Jeng (1994). The former developed a model for pore pressures and stresses for harmonic bed pressures with a bed that is infinitely deep. Hsu and Jeng (1994) expanded upon this by allowing a finite bed depth, and allowing for anisotropic Darcy flow resistance.

Our analysis has a similar approach as Guest and Hay (2017), also assuming that the shear modulus G of the porous bed is comparatively large, meaning that we assume the bed to be fully rigid in comparison with the pore fluid. We model the pressure at any arbitrary depth \hat{z} as the sum of $2N + 1$ harmonic components:

$$p(\hat{z}, t) = \sum_{j=-N}^N p_j^*(\hat{z})e^{i\omega_j t}, \quad p(\hat{z}, t) \in \mathbb{R}, \quad (4)$$

where $p_j^*(\hat{z}) \in \mathbb{C}$ is the complex amplitude of wave component j at depth \hat{z} . Here ω_j is the angular frequency, linked to the wave number \tilde{k}_j by the dispersion relation $\omega_j^2 = g\tilde{k}_j \tanh(\tilde{k}_j \bar{h})$, with \bar{h} being the mean water depth where we use the average measured water depth and $g = 9.81$ m/s² is the gravitational acceleration. The theories of Yamamoto et al. (1978) and Hsu and Jeng (1994) give descriptions of these complex amplitudes p^* under different circumstances. We follow the description by Guest and Hay (2017) who use the approach of Yamamoto et al. (1978) and introduce a tuning parameter a (s/m²):

$$p_j^*(\hat{z}) = P_j^* \exp(-\tilde{k}'_j \hat{z}), \quad \tilde{k}'_j = \tilde{k}_j \left(1 + \frac{i\omega_j a}{\tilde{k}_j^2} \right)^{1/2}. \quad (5)$$

here $P_j^* \in \mathbb{C}$ describes the amplitude and phase for wave component j at the bed and a is a parameter describing the properties of the pore fluid. One can interpret a as the constant that describes the magnitude of the amplitude decay and time-lag, where larger values correspond to stronger amplitude decay and larger time-lags.

It remains to define the complex amplitudes P_j^* . We can define these using the measured surface elevations and assuming hydrostatic pressure ($p(0, t) = \rho_w g h$, with $\rho_w = 1,000$ kg/m³ being the density of water), which is acceptable since the waves are shallow water waves. This gives us the relation

$$p(0, t) = \sum_{j=-N}^N P_j^* e^{i\omega_j t}. \quad (6)$$

Finally, we calculate these complex amplitudes using the discrete Fourier transform.

In this study, we use the parameter a for calibration. As described by Guest and Hay (2017), a is defined as

$$a = \frac{\gamma}{k_c} \left(n\beta + \frac{1-2\nu}{2(1-\nu)G} \right), \quad (7)$$

where $\gamma = \rho_w g$ is the weight of the pore fluid, k_c is the hydraulic conductivity, ν is Poisson's ratio, n is the porosity and β is the compressibility of the pore fluid. The latter is largely dependent on the air content in the beach, increasing with larger air content (Guest & Hay, 2017). The parameter a also has a meaningful physical interpretation, relating the frequency-dependent pressure attenuation and shift to the bed properties. We discuss this further in Section 4.4.

The theory above can also be applied to model pressure gradients. Given that we assumed an isotropic soil/water mixture in the first place, we can express the vertical pressure gradient as taking the vertical derivative of Equation 4, and using the chain rule:

$$\frac{\partial p}{\partial \hat{z}} = \sum_{j=-N}^N -\tilde{k}'_j p_j^*(\hat{z}) e^{i\omega_j t}. \quad (8)$$

The Biot equations with a Darcy flow resistance are linear (assuming time-invariant material properties), so a linear superposition can be used to predict pressures for an arbitrary seabed pressure $p(0, t)$.

2.3. Shields Parameter

We will also study the effect vertical pressure gradients have on the sediment weight in the Shields parameter θ :

$$\theta = \frac{\tau / \rho_w}{g(s-1)d}, \quad (9)$$

where τ is the bed shear stress and $s = \rho_s / \rho_w$ is the specific gravity of sediment, and d is the particle diameter, here chosen as $d = D_{50}$.

To investigate the influence of the pressure gradient, we use the modified Shields parameter approach from Sumer et al. (2011):

$$\theta' = \frac{\tau / \rho_w}{g(s-1)d - g\left(\frac{\partial \bar{p}}{\partial \hat{z}}\right)d}. \quad (10)$$

In our analysis we will however not look at the Shields parameter directly, instead we recognize that

$$\theta \propto u|u|/(s-1) \quad (11)$$

$$\theta' \propto u|u|/\left((s-1) - \frac{\partial \bar{p}}{\partial \hat{z}}\right) \quad (12)$$

which enables us to analyze the effect of the added pressure gradient term, without the requirement of calculating a bed shear stress. We call the right sides in the relations (11) and (12) the transport mobility.

2.4. Metrics

We use two metrics to assess the model performance. We define the normalized Root-Mean-Squared-Error (nRMSE) as:

$$nRMSE = \frac{\sqrt{\frac{1}{N} \sum_i^N (y_{s,i} - y_{r,i})^2}}{s_r}, \quad (13)$$

where N is the number of samples, s_i is the $y_{s,i}$ -th sample, $y_{r,i}$ is the i th reference value and s_r is the sample standard deviation defined as

$$s_r = \sqrt{\frac{1}{N} \sum_i^N (y_{r,i} - \bar{y}_r)^2}, \quad (14)$$

where \bar{y}_r is the mean of y_r . In the above equation, $y_{s,i}$ corresponds to modeled (sampled) values and $y_{r,i}$ refers to experimentally measured (reference) values. A low nRMSE value thus corresponds to small errors. Finally, the correlation between signals is measured using the Pearson's correlation coefficient r^2 .

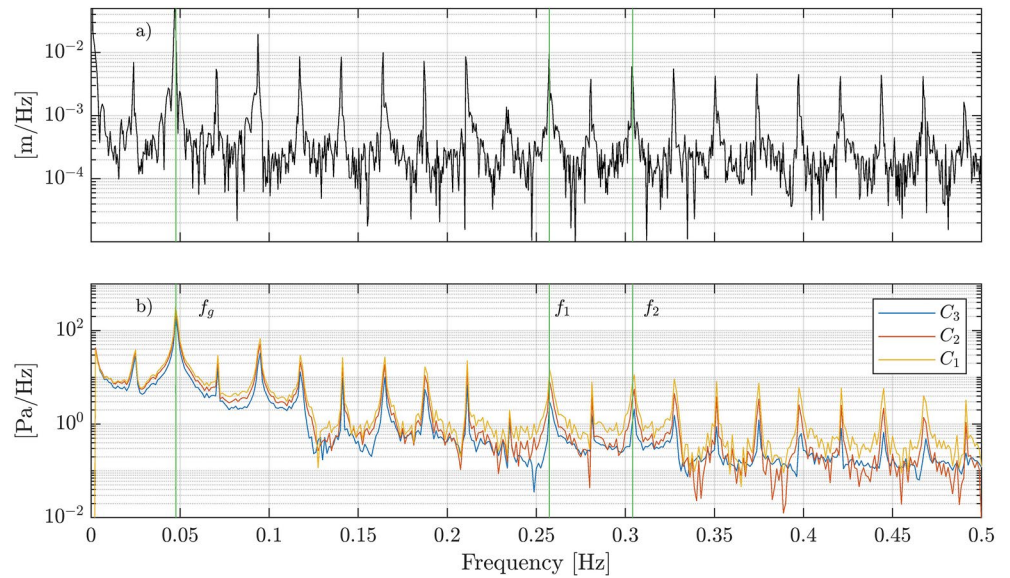


Figure 3. Spectrum showing the magnitude of the surface elevation (a) and the measured pressure in the bed (b) at location C. The green vertical lines show the group frequency f_g and the two bichromatic frequencies f_1 and f_2 .

3. Results

3.1. Pressure Observations

Figure 3 shows the amplitude spectrum of the surface elevation and the measured pressure at three depths at section C. The many peaks are harmonics of the bichromatic wave signal. The peak corresponding to the group frequency is highest in both panels. Comparing the amplitude spectrum of the surface elevation with the pressures, we can see that the surface elevation has more high frequency content than the pressure signals. Moreover, the deeper sensors show lower amplitudes compared with the shallowest sensor, especially at higher frequencies.

The short-wave peak corresponding to T_s (corresponding to a frequency of 0.286 Hz) does not appear large compared to neighboring peaks. Also the two peaks corresponding to the bichromatic wave components (0.257 and 0.304 Hz) are not considerably larger. This can be explained by the waves transforming while traveling from the paddle to the beach, and the waves breaking prior to the wave-gauges. The other peaks are harmonics and (partially) stem from interactions between the swash and incoming waves.

Figure 4 shows the observed water depths h , pressure deviations \bar{p} and pressure gradients between the sensors. The figure clearly shows the difference in hydrodynamical forcing, especially between location A and locations B and C. For instance, at locations B and C it is clearly visible that the bed becomes dry for extended periods between the wave groups (i.e., between $t = 1,252$ – $1,262$ s), whereas the dry periods at location A are considerably shorter (seen as the flat periods with $\eta = 0$). Furthermore, some waves recorded at location A are not recorded at locations B and C; for instance the middle wave group shows three distinct large peaks at location A but only one large and one small peak at locations B and C. This is probably due to wave-swash interactions in the lower swash, meaning that certain waves do not reach the upper locations or that waves have merged. Comparing locations B and C, the differences in water depth are small.

The pressure response (panels d–f) show similar trends at all three locations, that is, amplitude decay and a time lag that increases with the burial depth of the sensor. Note that at the three locations, the sensors are buried at different depths, meaning we cannot directly compare the amplitudes between the locations. Lastly the pressure gradients are calculated using Equation 3 and shown in panels (g–i). At all three locations we see positive pressure gradients (i.e., overpressure deeper in the bed, corresponding to upward seepage) during the dry phase between wave groups, and negative pressure gradients during the presence of waves. Location C shows the expected behavior according to the theory of Yamamoto et al. (1978), where the pressure gradient calculated closer to the bed surface has larger amplitude. However, at location B this does not seem to be the case as the pressure gradient between probes B2 and B3 display a smaller amplitude compared to the other two gradients. This is further discussed in Section 4.2.

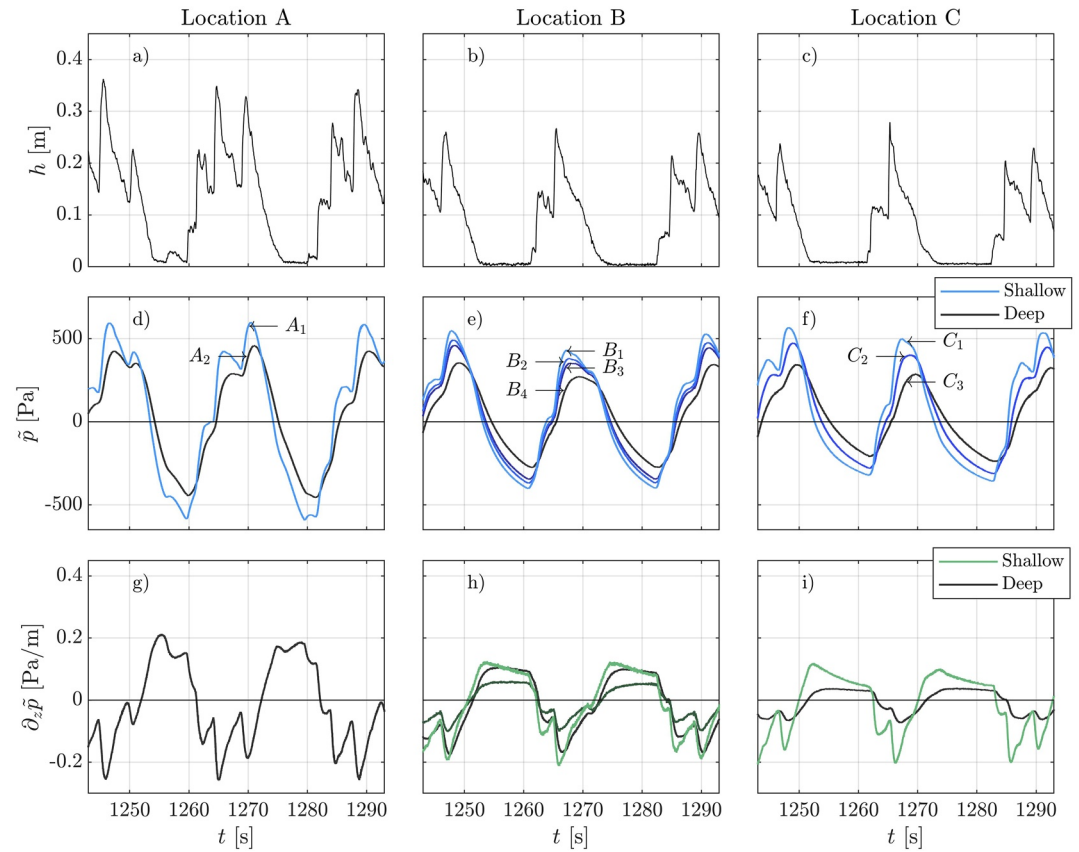


Figure 4. Figure showing the measured water depth (panels a to c), pressure deviation (panels d–f) and calculated pressure gradient according to Equation 3 (panels g–i). For panels d–i, the colors scale from the deepest sensor (dark) to the shallowest sensor (light). The arrows in panels (d–e) show the sensor corresponding to the line pointed to.

3.2. Model Calibration

The pressure model features one constant a that requires calibration. Since this constant is linked to physical properties of the beach that can differ per location, the calibration is done once for every cross-shore location. The calibration is based on the nRMSE values of the pressures (only pressures were used, not pressure gradients). Specifically, the individual nRMSE values, corresponding to each probe, were squared and minimized. The result of the calibration, and its corresponding nRMSE and r^2 values for both the pressure and the pressure gradients can be seen in Table 2. It is interesting to note that the calibration for location A, which is the most seaward location, has the lowest values of a . This will be discussed further in Section 4.4.

Table 2
Statistical Metrics Comparing the Modeled and Measured Pressure Signals, as Well as the Calculated and Modeled Pressure Gradients (Shown in Between the Sensors)

| Sensor nr | Location A | | Location B | | | | Location C | | |
|-------------------------|------------|-------|------------|-------|-------|-------|------------|-------|-------|
| | 1 | 2 | 1 | 2 | 3 | 4 | 1 | 2 | 3 |
| a (s/m ²) | 25.9 | | 37.7 | | | | 39.6 | | |
| nRMSE (–) | 0.223 | 0.178 | 0.186 | 0.185 | 0.197 | 0.199 | 0.129 | 0.101 | 0.432 |
| R^2 (–) | 0.95 | 0.98 | 0.97 | 0.97 | 0.96 | 0.96 | 0.99 | 0.99 | 0.93 |
| Grad nRMSE (–) | 0.328 | | 0.278 | 0.993 | 0.232 | 0.286 | | 0.784 | |
| Grad R^2 (–) | 0.91 | | 0.93 | 0.92 | 0.95 | 0.96 | | 0.99 | |

Note. The calibration for a is done for each location, as explained in Section 3.2.

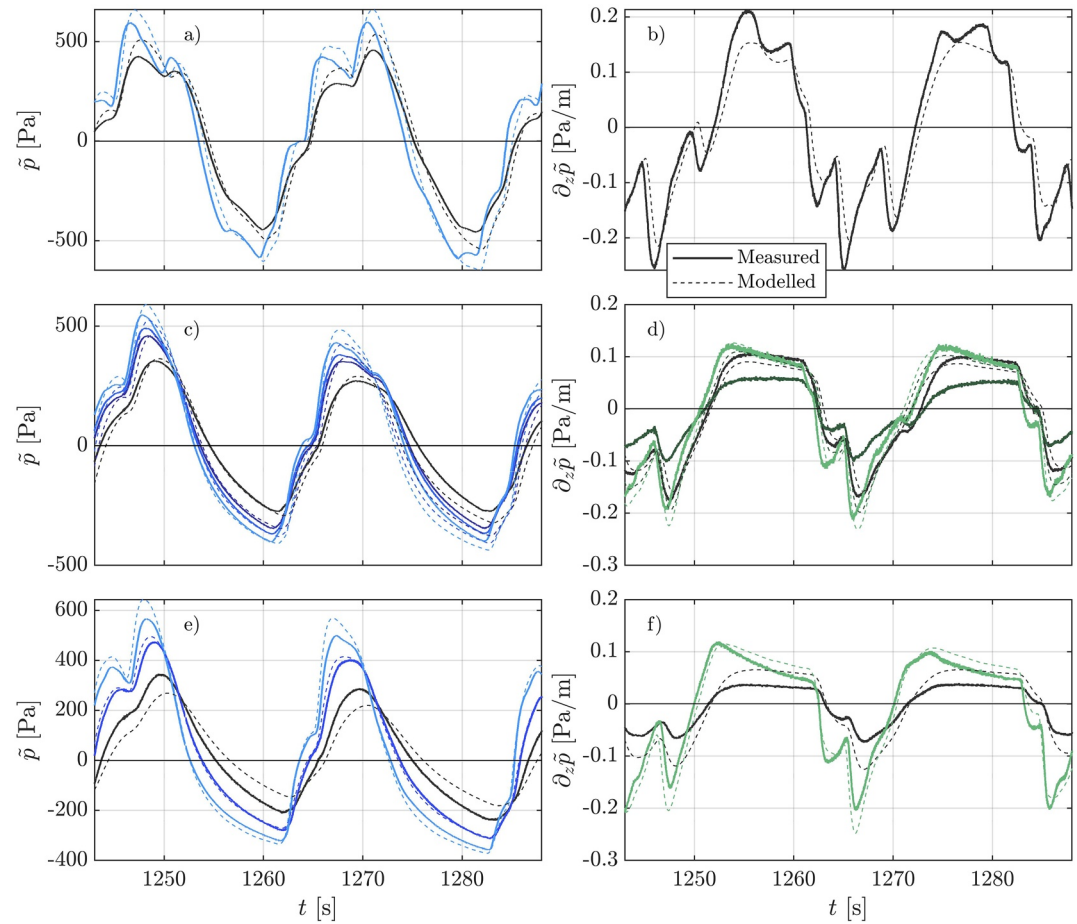


Figure 5. Snapshot of measured and modeled pore pressures (panels a, c, e) and estimated and modeled pressure gradients (panels b, d, f) using Equation 3. The continuous lines show measured results and the dashed lines show modeled results. The brightness of the colors are an indication of the depth, where the lighter colors correspond to locations closer to the bed surface. Panels a–f correspond to locations A, B, and C respectively.

Panels a, c, and e in Figure 5 compare the measured and modeled pressures. It is clear that the overall pressure behavior is modeled well (see also Table 2). At all three locations, the modeled pressures corresponding to the shallower burial depths seem to slightly overpredict the pressures, which is most pronounced for the most shallow probe at location C. This overshoot could possibly be explained by the bed level changing, and is discussed further in Section 4.3. Furthermore, the phasing of the modeled pressures generally corresponds well to the measured signals. However, especially at location A there is a small lag between the modeled and measured signals.

Panels b, d and f show a comparison between the modeled and measured pressure gradients. Again the modeled pressure gradients correspond well to the measured gradients. Location C shows somewhat overpredicted pressure gradients, which mirrors the overpredicted amplitude of the pressure while location A shows a well-modeled pressure gradient. At Location B the model results deviate more from the measurements. This is further discussed in Section 4.2.

The model captures both the quick response to the rapidly increasing water depth as a wave arrives, as well as the slow pressure decay during dry periods at Locations B and C. The same can be said for the pressure gradient behavior, where, even though the modeled magnitude is slightly off, the pressure gradient closer to the bed surface displace more rapid decay compared with the pressure gradient deeper in the bed.

3.3. Applying the Model

The model can be used to give insight into how specific wave frequencies influence the pressure in the bed. Panels a and b in Figure 6 show how the two different frequency components (a short-wave frequency and

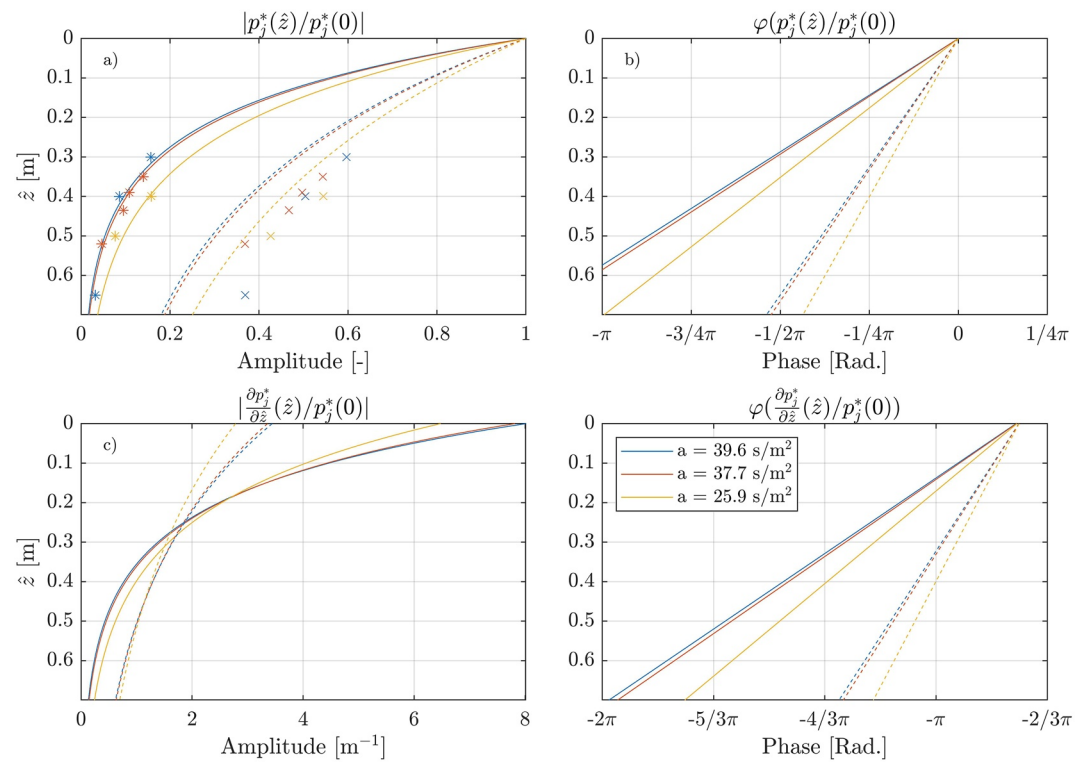


Figure 6. Figure showing the amplitude (a) and phase (b) of $p_j^*(\hat{z})/p_j^*(0)$ and amplitude (c) and phase (d) for $\frac{\partial p_j^*}{\partial \hat{z}}/p_j^*(0)$, for different chosen frequencies. Here the amplitude is denoted with $|\cdot|$ and the phase with $\varphi(\cdot)$. This is shown for the three different values of a that gave the best fit for the three sections. The continuous line corresponds to one of the bichromatic waves ($T = 3.88$ s) and the dashed line corresponds to the wave group ($T_g = 21.35$ s). Note, the x axes are different for different panels. The amplitude decay of the measurements are plotted in panel (a), where the stars correspond to the high frequency and crosses correspond to the group frequency.

the group frequency) are transferred into the bed, and how this signal is attenuated and displaced. The higher values of a clearly lead to stronger decay and larger time lags. Also, higher frequencies are attenuated quicker compared with lower frequencies, that penetrate further through the bed with a smaller time-delay. This is because the vertical scale is dictated by k' . Panel a also shows the measured amplitude decay of the two frequencies. This aligns well with the model for the higher frequency component. For the group frequency component, the measurements show slightly less decay compared with the model prediction. Panels c and d show the amplitude and phase of the pressure gradient (relative to a given pressure p_0 at the bed). It is clearly visible that higher frequency wave-components have a larger influence on the pressure gradient at the bed, however, around $\hat{z} < 0.25$ m this reverses, and the group-frequency component penetrates further into the bed. Note that this depth depends on both wave properties and bed properties. The phase shows the same frequency dependency for the gradient as for the pressure. However, the phase at $\hat{z} = 0$ is different, namely approximately $-3\pi/4$. As Guest and Hay (2017) showed, $\varphi(\tilde{k}') \approx \pi/4$, because $i\omega a/\tilde{k} \gg 1$. This means that $\varphi(-\tilde{k}') \approx -3\pi/4$.

The model provides a means to calculate pressure gradients at the bed surface by using Equation 8. Panels d to f in Figure 7 show the modeled pressure gradient, normalized with the specific weight of water $\gamma = \rho_w g$, at 1 cm below the bed. This is because the modeled signal at the bed ($z = 0$) shows some high-frequency noise which makes interpreting the signal more difficult. The pressure near the bed clearly contains more high-frequency content, due to the amplitude of the pressure gradient increasing with higher frequencies at the bed surface. At all three locations, the pressure gradient features strong negative spikes that coincide with instantaneous increases in water depth. These moments correspond to broken bores arriving at the particular location, and shows that these bores have an immediate and pronounced influence on the pressure gradient in the top layer of the soil. The maximum positive pressure gradient at the locations are roughly 0.5 (non-dimensional) for section A, and 0.4

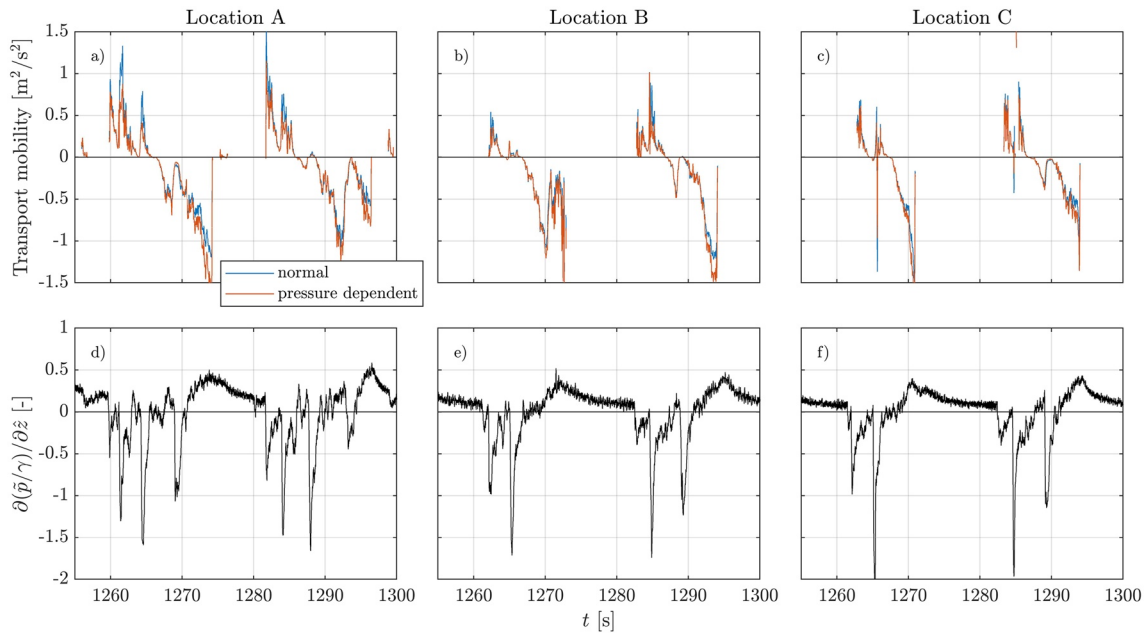


Figure 7. Figure showing the measured cross-shore squared velocities (panels a–c) where the blue line is the raw squared velocity and the red line incorporated the pressure correction as described in relations (11) and (12) and modeled vertical pressure gradients (panels d–f) at the three different cross-shore locations at 1 cm below the bed. Here positive transport mobilities correspond to onshore-directed transport, and negative transport mobilities corresponds to offshore-directed transport.

for sections B and C. This corresponds well with the measurements of Sumer et al. (2013) who recorded similar non-dimensional pressure gradients at similar locations.

Panels a to c give an indication of the effect the pressure gradient has on the Shields parameter, by looking at the transport mobility defined by relations (11) and (12). This is shown both raw and corrected for the pressure. For both signals, positive velocities accounted to a shoreward (uprush) motion. At all three sections the particle weight is increased during uprush, meaning that the effective Shields parameter is lower. Especially at location A during the uprush, the Shields parameter is momentarily almost halved due to this effect. During the backwash however, the particle weight is lower, leading to a higher off-shore directed Shields number. We will discuss these results and their limitations further in Section 4.5.

4. Discussion

4.1. Comparison With Other Studies

The measurements in this study complement the findings of Guest and Hay (2017) (mixed sand and gravel bed with $D_{50} \approx 5$ mm) that vertical pressure attenuation and phase shifting also play an important role for the pore-pressure behavior in a sandy bed. Interestingly, this contradicts the findings of Raubenheimer et al. (1998), who measured pore pressure gradients on a natural beach with $D_{50} = 0.2$ mm, very similar to the sediment used in this study. They did not find considerable phase shifts in their data. This could partially be explained by the fact that their study sampled the pressure at 2 Hz, which is considerably lower than in our study (100 Hz), and they analyzed components with frequencies of around 0.2 Hz and lower. However, the recent studies of Stark et al. (2022), analyzing pore pressures on a beach consisting of medium/coarse sand, and Florence et al. (2022), measuring pore pressures under storm conditions, confirm that phase-shifting plays a crucial role in explaining large pore-pressures. This is in line with our conclusion that the pressure measurements clearly display rapid attenuation and phase shifts. We conclude that in order to understand pore-pressure fluctuations on intraswash timescales, it is important to include the effect of phase shifts and additional attenuation due to the presence of compressible gas in the pore fluid.

4.2. Measurement Limitations

There are some limitations to the presented measurements. Due to the pressure attenuation and the burial depth of the pressure sensors, certain high-frequency or short-lived phenomena were not captured in these measurements. Sumer et al. (2011, 2013) directly measured the effect of vortices induced by wave-breaking, and their effect on the pore-pressure immediately below the bed surface. The morphodynamic variability of the bed during longer experiments makes determining a priori burial depths difficult, especially close to the bed surface. For future experiments, a setup that can be vertically adjusted during experiments such as the one by Baldock et al. (2001) might be more suited for this. Moreover, no porosity or saturation data was obtained during the experiments. As noted by other studies (for instance Mory et al. (2007) and Michallet et al. (2009)), there are key parameters determining the pressure response in the bed. These are also key parameters in the definition of a (see Equation 7). As such, when we are discussing the interpretation of the value of a , it is important to keep in mind that this is purely based on a comparison of timeseries in pressure, not based on a calculation based on bed properties.

The experimental campaign experienced some challenges that influence the results. The most apparent one is the effect of scour near instruments. This is a known effect for probes mounted from above (see for instance Sumer et al. (2013).) The scour depth was measured to be $\mathcal{O}(1 - 5 \text{ cm})$, depending on location. The combined effects of the scour and the overall morphodynamics meant that the top two sensors in the surf section were exposed and hence needed to be taken out. Furthermore, one sensor malfunctioned while buried. This meant that two locations had fewer sensors than originally planned (four sensors at every cross-shore location). Nonetheless, the data captured provides useful insight into the behavior of the pore pressure around the shoreline location.

Another issue has to do with the unexpected observation that the difference in pressure between the middle two probes at location B was very low, leading to a small measured pressure gradient. This becomes more apparent when comparing this with the modeled pressure gradient (Figure 5, panel (d)), where the modeled pressure gradient shows the expected amplitude decay whereas the measured pressure gradient does not. Also the associated nRMSE for the pressure gradient is very large at this location. A possible explanation for this could be interference between instruments, as the instruments were installed in close proximity to each other and attached to the same pole.

4.3. Analytical Model Performance

The analytical model used in this paper gives insight into the pressure propagation from the waves into the bed. The model performs well, in the sense that it can reproduce the pressure time-series reasonably well. This is backed up by the statistical metrics where most instruments display an nRMSE lower than 0.2 and an R^2 higher than 0.95. Only the shallowest swash probe displays considerably larger nRMSE of 0.4–0.6, depending on the run. Similarly, the model reproduces the pressure gradients reasonably well, except for location B for the aforementioned reasons (see Section 4.2).

It is important to consider the assumptions the model relies on, and the implications for the interpretations. First and foremost, the modification of Guest and Hay (2017) assumes $G\beta' \gg 0$, which means that the stiffness of the porous bed matrix should be much higher than the compressibility of the pore fluid. Here β' is the compressibility of water. In our case, $G\beta' \approx 300$, making it safe to assume that the model can be applied. Furthermore, the model assumes vertically homogeneous sediment properties, such as grain size, saturation and compactness. These might be more applicable to a laboratory environment compared with natural beaches. Nonetheless, Guest and Hay (2017) and Baldock et al. (2001) show that models assuming vertically uniform sediment properties can model the pressure behavior in the field. Furthermore, as also mentioned by Baldock et al. (2001), because the model is based on the pressure from the surface elevation only, non-hydrostatic effects are not taken into account. Such effects have been observed in the small-scale laboratory experiments by Sumer et al. (2011, 2013), who observed that individual eddies, originated from a broken wave, can lead to large ($\mathcal{O}(\partial\gamma\bar{p}/\partial\hat{z}) > 1$) positive pressure gradients near the bed surface responsible for rapid sediment suspension. These latter mentioned effects cannot be modeled using linear wave-theory and hence are not incorporated in the present study. However, if one assumes that the dynamics in the bed still can be described by linear Biot theory, a description of p_0 including the effects from nonlinear flow phenomena is sufficient.

Another assumption made by Yamamoto et al. (1978) is that the bed has an infinite depth. Since the flume has a depth of 2.5 m this assumption is clearly violated. The model by Hsu and Jeng (1994) provides a solution

which incorporates a finite depth of the bed. However, this model does not allow the simplification Guest and Hay (2017) suggested. We can estimate the importance of the finite depth by investigating the amplitude of the pressure and pressure gradients for different wave components at the flume wall. Using the lowest value of a between the sections, corresponding to the lowest damping, we can estimate that $(p^*/p_0^*)|_{z=2.47\text{m}} = 0.008$ and $(\partial p^*/\partial z)/p_0^*|_{z=2.47\text{m}} = 0.021\text{m}^{-1}$ for the wave-group component. All higher frequency components will thus have smaller amplitudes at this depth (for the short-wave component T_s these are $(p^*/p_0^*)|_{z=2.47\text{m}} = 4.8 \cdot 10^{-6}$ and $(\partial p^*/\partial z)/p_0^*|_{z=2.47\text{m}} = 3.3 \cdot 10^{-5}\text{m}^{-1}$). This shows that the effect of the finite depth is small. This is especially the case closer to the bed surface and for higher frequencies. Finally, it is important to consider that the model assumes a fixed bed, whereas the bed in the experiments is not fully static. For instance, intra-swash morphodynamics can be on the order of centimeters in seconds (Van der Zanden et al., 2015). Additionally, the locally observed scour observed during the experiment means that the bed level at the locations of the probes could be somewhat lower than recorded with the profiler. This could explain why for location C, the modeled pressure had an overpredicted amplitude for the top sensor, and an underpredicted amplitude for the bottom sensor.

4.4. Interpretation of Variability in a

The value of a at Location A differs from the considerably larger values at Location B ($a_C/a_A \approx 1.53$). Using Equation 7, we can try to explain this difference in the value of a using physical bed properties.

For instance, one argument uses that k_c is sensitive to the local packing (Van Gent, 1995) following the relation

$$k_c \propto \frac{n^3}{(1-n)^2}. \quad (15)$$

Keeping everything except k_c constant, the value of a depends strongly on the local packing. As an example, consider the porosity being $n_A = 0.40$ at Location A and $n_C = 0.35$. This would then lead to

$$\frac{1}{k_{cC}} / \frac{1}{k_{cA}} = 1.75, \quad (16)$$

which combined with the fact that a is inversely proportional to k_c , more than explains the ratio between a_C and a_A .

Another possible difference between the locations is the local air content in the bed. In Equation 7, the compressibility is determined by the saturation of the bed (Verruijt, 1969):

$$\beta = S\beta' + \frac{1-S}{P_{atm}}, \quad (17)$$

where P_{atm} is the atmospheric pressure at the surface level. If we keep k_c constant and change the local bed saturation, we find that lowering the air content, meaning the saturation is higher, leads to a lower value of a . This explains the lower value of a at Location A compared with B and C, as this location is more offshore located where one would expect lower air content in the bed compared to more onshore locations. A future experimental study with co-located measurements of air content and pore-pressures in the swash zone would be very interesting. It is important to note that a here is taken as the average over the whole analysis time-series. In reality, this parameter is not constant and changes in bed properties such as saturation and compaction during the experiment can occur.

Compared to Guest and Hay (2017), the value of a in our study is an order of magnitude higher (between $a = 25\text{ s/m}^2$ and $a = 40\text{ s/m}^2$ compared to $a = 2.9\text{ s/m}^2$). Using similar arguments as above, this difference can be explained by the difference in bed composition and its effects on the hydraulic conductivity and saturation.

4.5. Implications for Sediment Transport

Figure 7 shows the nondimensionalized pressure gradient $\frac{\partial p/\gamma}{\partial z}$ varying between approximately 0.5 and -2 at different stages in during the swash motion. This has a substantial impact on the transport mobility (Figure 8).

This shows that at these different stages, the transport mobility (according to this formulation) can vary by almost a factor 3 depending on the pressure gradient alone.

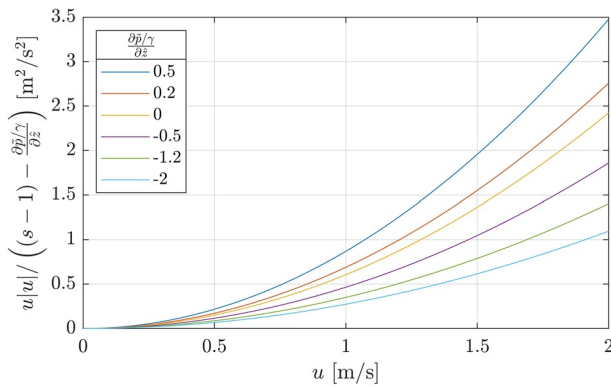


Figure 8. The effect of the nondimensionalized pressure gradient $\frac{\partial p/\gamma}{\partial z}$ at different velocities on the transport mobility as defined in Equation 12.

In the context of sediment transport, it is important to note that there is a discussion about the validity of incorporating the change to the apparent weight due to vertical pressure gradients in the Shields description (Baldock & Nielsen, 2010; Francalanci et al., 2010), particularly when it comes to bedload transport. Baldock and Nielsen (2010) argue (amongst other things) that the additional seepage-related force only acts within the bed, whereas for particles outside the bed the pressure gradient is essentially zero. However, Francalanci et al. (2010) argue that the pressure gradient does influence particle entrainment, and thus sediment transport in general. Regardless of the discussion, Baldock and Nielsen (2010) note that the vertical pressure gradient can influence the sheet flow layer and experiments by Sumer et al. (2013) show that pressure gradients can lead to rapid suspension events. Keeping these points in mind, we believe that the Shields parameter provides a useful metric to analyze the impact of pressure gradients on sediment transport.

In this paper, we chose to limit the analysis to the effective particle weight using the approach of Sumer et al. (2011). An alternative is the approach by Yeh and Mason (2014), where also the porosity of the bed is accounted for:

$$\theta'_n = \frac{\tau(1-n)/\rho_w}{g(s-1)(1-n)d - g\left(\frac{\partial p/\gamma}{\partial z}\right)d}, \quad (18)$$

Without pressure gradients, these two formulations default back to the Shields parameter in Equation 9. An interpretation of the (Yeh & Mason, 2014) approach is that their Shields parameter (Equation 18) addresses the bulk stability of the soil whereas the (Sumer et al., 2011) approach (Equation 10) addresses the stability of individual grains. As the difference effectively only comes down to scaling the relative effect of the pressure gradient, we do not believe the choice of Shields parameter affects our conclusions.

Modeling the effect of vertical pressure gradients is not limited to modifying the effective sediment weight in the Shields parameter. For instance, one can modify the critical Shields stress (N. S. Cheng & Chiew, 1999), or modify the Shields parameter to include effects on the boundary layer through infiltration, possibly in conjunction with the modified sediment weight (Anderson, 2015; Conley & Inman, 1994; Francalanci et al., 2008; Nielsen et al., 2001). This boundary layer effect has the opposite effect to the modified particle weight, leading to increased friction during uprush and decreased friction during the backwash. In fact, Lohmann et al. (2006) found this to be the dominant effect of the two, meaning that infiltration increased bed friction and exfiltration decreased bed friction. However, using any of the approaches mentioned above, the friction velocity related to the boundary layer shape, is needed. To estimate this from measurements would require even more approximations, which would lead to large uncertainties. For this reason, we stuck to the approach of modifying the effective sediment weight. Now that there exist models that can resolve the detailed flow in the swash zone and model sediment transport and morphodynamics (e.g., Z. Cheng et al., 2017; Kim et al., 2019; Kranenborg et al., 2022), numerical models can be great tools for analyzing the aforementioned effects in detail, and investigate their relative importance for sediment transport under different conditions.

5. Conclusion

In this study, we investigated the behavior of pore pressure at different depths in the bed, under the forcing of bichromatic waves. To do this, new field-scale laboratory measurements of pore pressures at different depths, surface elevations and flow velocities were conducted. These measurements were used to calibrate an analytical model, which allowed further analysis of the pore pressure behavior. The main conclusions are summarized as follows:

- The measurements clearly show that, for intraswash timescales, the pressure propagation in the bed is frequency dependent. Specifically, lower frequencies penetrate deeper into the bed and shift less, whereas higher frequencies experience more damping and larger phase shifting. This is in agreement with previous studies, for example, Guest and Hay (2017) and Stark et al. (2022).

- An analytical model, based on the theory of Yamamoto et al. (1978) and Guest and Hay (2017), was able to reproduce the pressure and pressure gradient well for all three cross-shore locations. Instead of basing the model on bed properties such as porosity and saturation, the model uses a single model coefficient a which is calibrated using time-series of the pressure.
- Despite the recurring covering and uncovering of the bed and uncertainties in the bed saturation, the analytical model, based on the assumption that the bed is vertically uniform and always covered by water, is able to predict the pressure behavior in the bed.
- The calibrated model value a was highest for the most onshore measurement location, and the lowest for the most offshore location. This variation of a could possibly be explained in terms of local bed packing and bed saturation. This shows that it might be possible to estimate such bed properties indirectly by measuring pore pressure and calculating corresponding values of a .
- During the backwash, the modeled effective sediment weight is increased due to the gradients. During the uprush, the pressure gradient has the opposite effect where the submerged weight is reduced significantly.

Data Availability Statement

Data and code is publicly available for download at <https://zenodo.org/record/8301244>.

Acknowledgments

We would like to thank prof. K.M. Wijnberg for aiding with the supervision of T. Pauli during his Msc. thesis. We would also like to thank the two anonymous reviewers for their constructive feedback to the manuscript. This work is part of the research program Shaping The Beach with project number 16130, which is financed by the Netherlands Organisation for Scientific Research (NWO), with in-kind support by Deltares.

References

- Anderson, W. P. (2015). Coastal groundwater. In *Coastal Environments and Global Change* (pp. 128–148). <https://doi.org/10.1002/9781117261.ch6>
- Baldock, T. E., Baird, A. J., Horn, D. P., & Mason, T. (2001). Measurements and modeling of swash-induced pressure gradients in the surface layers of a sand beach. *Journal of Geophysical Research*, *106*(C2), 2653–2666. <https://doi.org/10.1029/1999jc000170>
- Baldock, T. E., & Holmes, P. (1998). Seepage effects on sediment transport by waves and currents. In *Proceedings of the coastal engineering conference* (Vol. 3, pp. 3601–3614). American Society of Civil Engineers. <https://doi.org/10.1061/9780784404119.274>
- Baldock, T. E., & Nielsen, P. (2010). Discussion of “Effect of seepage-induced nonhydrostatic pressure distribution on bed-load transport and bed morphodynamics” by Simona Francalanci, Gary Parker, and Luca Solari. *Journal of Hydraulic Engineering*, *136*(1), 77–79. [https://doi.org/10.1061/\(asce\)hy.1943-7900.0000015](https://doi.org/10.1061/(asce)hy.1943-7900.0000015)
- Biot, M. A. (1941). General theory of three-dimensional consolidation. *Journal of Applied Physics*, *12*(2), 155–164. <https://doi.org/10.1063/1.1712886>
- Butt, T., Russell, P., & Turner, I. (2001). Influence of swash infiltration–exfiltration on beach sediment transport: Onshore or inshore? *Coastal Engineering*, *42*(1), 35–52. [https://doi.org/10.1016/s0378-3839\(00\)00046-6](https://doi.org/10.1016/s0378-3839(00)00046-6)
- Cheng, N. S., & Chiew, Y. M. (1999). Incipient sediment motion with upward seepage. *Journal of Hydraulic Research*, *37*(5), 665–681. <https://doi.org/10.1080/00221689909498522>
- Cheng, Z., Hsu, T. J., & Calantoni, J. (2017). SedFoam: A multi-dimensional Eulerian two-phase model for sediment transport and its application to momentary bed failure. *Coastal Engineering*, *119*, 32–50. <https://doi.org/10.1016/j.coastaleng.2016.08.007>
- Conley, D. C., & Inman, D. L. (1994). Ventilated oscillatory boundary layers. *Journal of Fluid Mechanics*, *273*(C6), 261–284. <https://doi.org/10.1017/S002211209400193X>
- Florence, M., Stark, N., Raubenheimer, B., & Elgar, S. (2022). Nearshore vertical pore pressure gradients and onshore sediment transport under tropical storm forcing. *Journal of Waterway, Port, Coastal, and Ocean Engineering*, *148*(6), 04022023. [https://doi.org/10.1061/\(ASCE\)WW.1943-5460.0000723](https://doi.org/10.1061/(ASCE)WW.1943-5460.0000723)
- Francalanci, S., Parker, G., & Solari, L. (2008). Effect of seepage-induced nonhydrostatic pressure distribution on bed-load transport and bed morphodynamics. *Journal of Hydraulic Engineering*, *134*(4), 378–389. [https://doi.org/10.1061/\(asce\)0733-9429\(2008\)134:4\(378\)](https://doi.org/10.1061/(asce)0733-9429(2008)134:4(378))
- Francalanci, S., Parker, G., & Solari, L. (2010). Closure to “Effect of seepage-induced nonhydrostatic pressure distribution on bed-load transport and bed morphodynamics” by Simona Francalanci, Gary Parker, and Luca Solari. *Journal of Hydraulic Engineering*, *136*(1), 79–82. [https://doi.org/10.1061/\(asce\)hy.1943-7900.0000160](https://doi.org/10.1061/(asce)hy.1943-7900.0000160)
- Fredsøe, J., Sumer, B. M., Kozakiewicz, A., Chua, L. H., & Deigaard, R. (2003). Effect of externally generated turbulence on wave boundary layer. *Coastal Engineering*, *49*(3), 155–183. [https://doi.org/10.1016/S0378-3839\(03\)00032-2](https://doi.org/10.1016/S0378-3839(03)00032-2)
- Guest, T. B., & Hay, A. E. (2017). Vertical structure of pore pressure under surface gravity waves on a steep, megatidal, mixed sand-gravel-cobble beach. *Journal of Geophysical Research: Oceans*, *122*(1), 153–170. <https://doi.org/10.1002/2016JC012257>
- Heiss, J. W., Ullman, W. J., & Michael, H. A. (2014). Swash zone moisture dynamics and unsaturated infiltration in two sandy beach aquifers. *Coastal and Shelf Science*, *143*, 20–31. <https://doi.org/10.1016/j.cess.2014.03.015>
- Horn, D. P. (2002). Beach groundwater dynamics. *Geomorphology*, *48*(1–3), 121–146. [https://doi.org/10.1016/S0169-555X\(02\)00178-2](https://doi.org/10.1016/S0169-555X(02)00178-2)
- Horn, D. P. (2006). Measurements and modelling of beach groundwater flow in the swash-zone: A review. *Continental Shelf Research*, *26*(5), 622–652. <https://doi.org/10.1016/j.csr.2006.02.001>
- Hsu, J. R. C., & Jeng, D. S. (1994). Wave-induced soil response in an unsaturated anisotropic seabed of finite thickness. *International Journal for Numerical and Analytical Methods in Geomechanics*, *18*(11), 785–807. <https://doi.org/10.1002/nag.1610181104>
- Kim, Y., Mieras, R. S., Cheng, Z., Anderson, D., Hsu, T. J., Puleo, J. A., & Cox, D. (2019). A numerical study of sheet flow driven by velocity and acceleration skewed near-breaking waves on a sandbar using SedWaveFoam. *Coastal Engineering*, *152*, 103526. <https://doi.org/10.1016/j.coastaleng.2019.103526>
- Kranenborg, J. W. M., Campmans, G. H. P., Jacobsen, N. G., Van der Werf, J. J., Reniers, A. J. H. M., & Hulscher, S. J. H. M. (2022). Depth-resolved modelling of intra-swash morphodynamics induced by solitary waves. *Journal of Marine Science and Engineering*, *10*(9), 1175. <https://doi.org/10.3390/jmse10091175>
- Lohmann, I. P., Fredsøe, J., Sumer, B. M., & Christensen, E. D. (2006). Large eddy simulation of the ventilated wave boundary layer. *Journal of Geophysical Research*, *111*(6), C06036. <https://doi.org/10.1029/2005JC002946>

- Masselink, G., & Li, L. (2001). The role of swash infiltration in determining the beachface gradient: A numerical study. *Marine Geology*, 176(1–4), 139–156. [https://doi.org/10.1016/S0025-3227\(01\)00161-X](https://doi.org/10.1016/S0025-3227(01)00161-X)
- Michallet, H., Mory, M., & Piedra-Cueva, I. (2009). Wave-induced pore pressure measurements near a coastal structure. *Journal of Geophysical Research*, 114(C6), C06019. <https://doi.org/10.1029/2008JC005071>
- Mory, M., Michallet, H., Bonjean, D., Piedra-Cueva, I., Barnoud, J. M., Foray, P., et al. (2007). A field study of momentary liquefaction caused by waves around a coastal structure. *Journal of Waterway, Port, Coastal, and Ocean Engineering*, 133(1), 28–38. [https://doi.org/10.1061/\(ASCE\)0733-950X\(2007\)133:1\(28\)](https://doi.org/10.1061/(ASCE)0733-950X(2007)133:1(28))
- Nielsen, P., Robert, S., Møller-Christiansen, B., & Oliva, P. (2001). Infiltration effects on sediment mobility under waves. *Coastal Engineering*, 42(2), 105–114. [https://doi.org/10.1016/S0378-3839\(00\)00051-X](https://doi.org/10.1016/S0378-3839(00)00051-X)
- Pedrozo-Acuña, A., Simmonds, D. J., & Reeve, D. E. (2008). Wave-impact characteristics of plunging breakers acting on gravel beaches. *Marine Geology*, 253(1–2), 26–35. <https://doi.org/10.1016/j.margeo.2008.04.013>
- Raubenheimer, B., Elgar, S., & Guza, R. T. (1998). Estimating wave heights from pressure measured in sand bed. *Journal of Waterway, Port, Coastal, and Ocean Engineering*, 124(3), 151–154. [https://doi.org/10.1061/\(ASCE\)0733-950X\(1998\)124:3\(151\)](https://doi.org/10.1061/(ASCE)0733-950X(1998)124:3(151))
- Sanchez-Arcilla, A., & Cáceres, I. (2018). An analysis of nearshore profile and bar development under large scale erosive and accretive waves. *Journal of Hydraulic Research*, 56(2), 231–244. <https://doi.org/10.1080/00221686.2017.1315748>
- Stark, N., Mewis, P., Reeve, B., Florence, M., Piller, J., & Simon, J. (2022). Vertical pore pressure variations and geotechnical sediment properties at a sandy beach. *Coastal Engineering*, 172, 104058. <https://doi.org/10.1016/j.coastaleng.2021.104058>
- Sumer, B. M., & Fredsøe, J. (2002). The mechanics of scour in the marine environment. In *Advanced series on ocean engineering publication title: Coastal engineering issue: 1* (Vol. 17). WORLD SCIENTIFIC. <https://doi.org/10.1142/4942>
- Sumer, B. M., Guner, H. A. A., Hansen, N. M., Fuhrman, D. R., & Fredsøe, J. (2013). Laboratory observations of flow and sediment transport induced by plunging regular waves. *Journal of Geophysical Research: Oceans*, 118(11), 6161–6182. <https://doi.org/10.1002/2013JC009324>
- Sumer, B. M., Sen, M. B., Karagali, I., Ceren, B., Fredsøe, J., Sottile, M., et al. (2011). Flow and sediment transport induced by a plunging solitary wave. *Journal of Geophysical Research*, 116(1), 1–15. <https://doi.org/10.1029/2010JC006435>
- Turner, I. L., & Nielsen, P. (1997). Rapid water table fluctuations within the beach face: Implications for swash zone sediment mobility? *Coastal Engineering*, 32(1), 45–59. [https://doi.org/10.1016/S0378-3839\(97\)00015-X](https://doi.org/10.1016/S0378-3839(97)00015-X)
- Van der Werf, J., Dionísio António, S., Kranenborg, J., Vermeulen, B., Campmans, G., van der Zanden, J., et al. (2019). Shaping the beach: Cross-shore sand transport in the swash zone. *Coastal Structures*, 2019, 851–861. https://doi.org/10.18451/978-3-939230-64-9_080
- Van der Zanden, J., Alsina, J. M., Cáceres, I., Buijsrogge, R. H., & Ribberink, J. S. (2015). Bed level motions and sheet flow processes in the swash zone: Observations with a new conductivity-based concentration measuring technique (CCM+). *Coastal Engineering*, 105, 47–65. <https://doi.org/10.1016/j.coastaleng.2015.08.009>
- Van der Zanden, J., Cáceres, I., Eichtopf, S., Ribberink, J. S., Van der Werf, J. J., & Alsina, J. M. (2019). Sand transport processes and bed level changes induced by two alternating laboratory swash events. *Coastal Engineering*, 152, 103519. <https://doi.org/10.1016/j.coastaleng.2019.103519>
- Van Gent, M. R. A. (1995). Porous flow through rubble-mound material. *Journal of Waterway, Port, Coastal, and Ocean Engineering*, 121(3), 176–181. [https://doi.org/10.1061/\(asce\)0733-950X\(1995\)121:3\(176\)](https://doi.org/10.1061/(asce)0733-950X(1995)121:3(176))
- Verruijt, A. (1969). Elastic storage of aquifers. In *Flow through porous media* (pp. 331–376). Academic Press.
- Yamamoto, T., Koning, H. L., Sellmeijer, H., & Van Hijum, E. V. (1978). On the response of a poro-elastic bed to water waves. *Journal of Fluid Mechanics*, 87(1), 193–206. <https://doi.org/10.1017/S0022112078003006>
- Yeh, H., & Mason, H. (2014). Sediment response to tsunami loading: Mechanisms and estimates. *Géotechnique*, 64(2), 131–143. <https://doi.org/10.1680/geot.13.P.033>